Biofilm 3 (2021) 100053

Contents lists available at ScienceDirect

Biofilm

journal homepage: www.sciencedirect.com/journal/biofilm

Kinetics and scale up of oxygen reducing cathodic biofilms

Abdelrhman Mohamed, Phuc T. Ha, Haluk Beyenal *

The Gene and Linda Voiland School of Chemical Engineering and Bioengineering, Washington State University, Pullman, WA, USA

ARTICLE INFO

Keywords:
Cathodic biofilms
Biocathodes
Scale up
Catalyzed oxygen reduction
Bioelectrochemical system

ABSTRACT

The goals of this work were to study the kinetics and investigate the factors controlling the scale up of oxygen reducing mixed culture cathodic biofilms. Cathodic biofilms were enriched on different electrode sizes (14.5 cm^2, 40.3 cm^2, 131 cm^2 and 466 cm^2). Biofilm enrichment shifted the oxygen reduction onset potential from −0.1 $V_{Ag/AgCl}$ to 0.3 $V_{Ag/AgCl}$, indicating the biofilm catalyzed oxygen reduction. The kinetics of oxygen reduction were studied by varying the bulk dissolved oxygen concentration. Oxygen reduction followed a Michaelis-Menten kinetics on all electrode sizes. The maximum current density decreased with increasing electrode surface area (−97.0 ± 10.6 μA/cm^2, −76.0 ± 8.2 μA/cm^2, −66.3 ± 3.0 μA/cm^2 and −43.5 ± 10.5 μA/cm^2, respectively). Cyclic voltammograms suggest that scale up was limited by ohmic resistance, likely due to the low ionic conductivity in the wastewater medium. Mathematical modeling using combined Michaelis-Menten and Butler-Volmer model supports that the decrease in current density with increasing electrode surface area is caused by ohmic losses. Analysis of the microbial community structure in different size electrodes and in multiple regions on the same electrode showed low variability, suggesting that the microbial community does not control the scale up of cathodic biofilms.

1. Introduction

The discovery of electrochemically-active biofilms (EABs) has spurred new promising applications in environmental biotechnology [1–4]. EABs are formed by microorganisms that attach to and exchange electrons with solid electrodes or minerals [5,6]. EABs can be anodic biofilms, i.e. using a solid electron acceptor, or cathodic biofilms, i.e. using a solid electron donor[7]. The unique ability of such EABs to exchange electrons with solid electrodes has been demonstrated in multiple bioelectrochemical systems. Microbial fuel cells (MFCs) produce electrical energy from organic sources by utilizing anodic biofilms in combination with cathodic biofilms or abiotic cathodes [8–11]. The utility of MFCs was demonstrated in a variety of applications, including reducing the energy requirements of wastewater treatment, electrical power generation in remote areas, and environmental sensing [12–18]. On the other hand, microbial electrolysis cells consume electrical energy to catalyze the production of chemicals of interest [19–21]. For example, microbial electrolysis cells were used for the production of hydrogen, biogas, ethanol and hydrogen peroxide [22–25]. In addition, bioelectrochemical systems utilizing anodic or cathodic biofilms have been demonstrated in other promising applications, such as environmental bioremediation, pollutant removal, and nutrient and metal recovery [26–30].

Applications utilizing EABs are typically demonstrated with promising results in small laboratory scales. Several studies demonstrated such applications in pilot scale [12,31–33]. However, these efforts have suffered from practical challenges associated with scaling up biofilm electrodes [34–37]. In a survey of literature, Dewan et al. documented the decrease of power density of MFCs with increasing anode surface area [34]. This observation was also corroborated in a controlled study utilizing *Shewanella oneidensis* MR-1 as the anodic biofilm [34]. A significant decrease in power density was also observed in a study investigating the scale up of sediment microbial fuel cells in the lab and in the field [35]. Recently, Tutar et al. investigated the scale up of a mixed culture wastewater anodic biofilms utilizing wastewater or wastewater amended with potassium acetate as the electron donor [38]. Interestingly, while anodes fed with municipal wastewater showed a decrease in current density with increasing electrode size, the anodes fed with acetate-amended wastewater maintained a similar anodic current density in all tested electrode sizes [38]. These results indicated that scale up could be controlled by the electron donor availability or the ionic conductivity of the electrolyte solution.

Several strategies have been proposed to mitigate the challenge of decreasing power densities at large scale systems by connecting multiple

* Corresponding author.
E-mail address: beyenal@wsu.edu (H. Beyenal).

https://doi.org/10.1016/j.biofilm.2021.100053
Received 3 February 2021; Received in revised form 5 May 2021; Accepted 1 June 2021
Available online 18 June 2021

smaller systems. MFC stacks have been tested in a parallel or series configurations to increase the system output potential or current, respectively [39–42]. Several challenges are documented during the operation of MFC stacks documented, including voltage reversal and potential losses in hydraulically-connected systems [43–45]. Novel approaches focusing on the architecture of MFC stacks or the electronics connected to the MFCs were reported to address these challenges [46–49]. In addition, promising strategies to increase the overall power production from multiple independent MFCs using novel electronic circuitry have been reported. It was demonstrated that harvesting power from independently operated MFCs and adding the harvested power electronically generated significantly higher power than a single equivalent MFC with the same total surface area, or MFCs operated in a parallel configuration [45]. A flyback converter circuitry was used to isolate and hold the voltage of individual MFCs at an optimum value (0.35–0.5 V) while increasing the output potential to 12 V to charge an energy storage device [50]. Regardless of the selected scale up strategy, practical implementation requires a compromise between the increased power density of using small systems and the added complexity associated with the number of units used. Understanding the factors controlling the scale up of biofilm electrodes is required to devise a rational design strategy to implement bioelectrochemical systems in practical applications.

Oxygen reduction reaction (ORR) is the primary cathodic reaction used in sediment microbial fuel cells (SMFCs). SMFCs can be limited by the cathodic reaction rate due to the high overpotential required for oxygen reduction [51–53]. The enrichment of cathodic biofilms have been demonstrated to catalyze the ORR in polarized cathodes and in MFCs [53–59]. Additionally, literature reports demonstrated the development of biocathodes for several processes including denitrification, carbon dioxide and perchlorate reduction, metal recovery, toxicity monitoring and biofilm monitoring [60–68]. While previous work has focused on the scale up of anodic biofilm systems, less attention has been paid to the scale up of cathodic biofilms. The goals of this work were to study the kinetics and investigate the factors controlling the scale up of cathodic biofilm electrodes. To our knowledge, this is the first study to focus on the kinetics and scale up of oxygen reducing cathodic biofilms under potentiostatic control. We enriched mixed culture cathodic biofilms catalyzing the ORR on various electrode sizes (14.5 cm^2, 40.3 cm^2, 131 cm^2 and 466 cm^2). After the enrichment, we studied the reaction kinetics and the effect of electron acceptor concentration on scale up by changing the dissolved oxygen (DO) concentration. The DO concentration was controlled by bubbling the electrolyte with O_2 and N_2 gas mixture at various partial pressures of oxygen. The steady-state response of the cathodic biofilms to change in DO concentration was used to study the kinetics of oxygen reduction on the different sized electrodes. Cyclic voltammograms recorded at multiple DO concentrations were used to provide an insight to the loss of current density at large electrodes. We used mathematical modeling to determine the factors contributing to the decrease in current density with increasing cathode surface area. Experimental data were fitted to a combined Michaelis-Menten and Butler-Volmer model to describe biologically catalyzed reactions and electrode kinetics. Finally, the analysis of the microbial community structure on cathodic biofilms enriched on different electrode sizes, and on multiple places within a single electrode provided was used to investigate the heterogeneity of cathodic biofilms and whether the microbial community changed as a result of enrichment on electrodes of different sizes.

2. Materials and methods

2.1. Electrochemical cell and electrode construction

The electrochemical cell used for the enrichment of cathodic biofilms is illustrated in the supplementary information (Fig. S1). Each reactor consists of a carbon fabric working electrode (Zoltek Companies Inc., St. Louis, MO, catalog #PX30FBPW06), a 6-mm-thick graphite felt counter electrode (HP Materials Solutions, Woodland Hills, CA), and an Ag/AgCl reference electrode. The reference electrode is manufactured in house according to previously published protocols [69]. All three electrodes are mounted on a hollow frame made from acrylic glass and cut using a laser cutter. Briefly, the frame allows fixing the electrode in place while keeping a constant distance of 1.3 cm between the working and counter electrodes. The reference electrode was fixed to the side of the acrylic frame, approximately 0.6 cm away from the working electrode.

Electrical connection to the working and counter electrodes was established using titanium wire (Malin Co., Cleveland, OH, 0.025-inch diameter, catalog #31262) woven through the electrodes and wrapped around the plastic screws used to fix the electrodes to the plastic frame. The pressure from tightening the screws into the plastic frame ensured good electrical contact between the titanium wire and the electrodes. Multiple contact points were used in each electrode. The titanium wires were soldered to insulated 18 AWG copper wires and sealed by insulating the solder junction with marine adhesive sealant (3 M 5200 Fast Cure, catalog #06535) following the manufacturer's instructions. The maximum electrical resistance between the copper wire and any point on the surface of the electrodes was below 1 Ω. If the resistance exceeded 1 Ω, the electrode assembly was discarded. The reference electrode was fixed to one side of the frame between the working and the counter electrode, with the porous frit located at the middle of the height of the working and counter electrodes (Fig. S1).

To study the scale up of cathodic biofilms, four electrode sizes with projected surface areas of 14.5 cm^2 (3.81 cm × 3.81 cm), 40.3 cm^2 (6.35 cm × 6.35 cm), 131 cm^2 (11.4 cm × 11.4 cm) and 466 cm^2 (21.6 cm × 21.6 cm) were used. The counter electrodes were made of graphite felt with the same projected surface area as the working electrode. Thus, the counter electrodes had higher surface areas in comparison to the working electrodes because graphite felt has higher specific surface area compared to the carbon fabric. Each set of electrodes (working, counter and reference electrodes) were housed in a separate reactor with a working volume of 7 L and operated at room temperature (average of 23 °C). The reactors were aerated by sparging air through a diffuser stone, with input air pressure of 13.8 kPa. The input air pressure was selected as further increase in pressure during preliminary experiments did not result in an increase in measured cathodic current or DO concentration (data not shown). This aerating strategy also ensured well-mixing of the liquid solution. The air inlet was bubbled through a water column to increase the moisture content of air, and minimize evaporation of medium. Experiments were repeated three times for each electrode size using new electrodes and fresh medium and inoculum. Data describing the cathode kinetics as a function of electrode size and DO concentration are reported as the average ± standard deviation of three independent biological replicates.

2.2. Enrichment of cathodic biofilms

The cathodic biofilms were enriched in municipal wastewater, diluted in tap water with a ratio of 1:7.3. The reactor was inoculated with mixed culture collected from wastewater treatment plant (10% of the reactor working volume). The initial pH of the mixture was 7.1 ± 0.1. Tap water and wastewater had a similar electrolytic conductivity range (400–500 μΩ/cm). Raw municipal wastewater and mixed culture were collected from the inlet to secondary treatment stage and from the anaerobic treatment basin of City of Moscow Water Reclamation and Reuse Facility, respectively (Moscow, ID, USA). This facility uses an enhanced biological phosphorus removal wastewater treatment process. Wastewater and mixed culture were collected from the wastewater treatment plant and used in experiments on the same day. Cathodic biofilms were enriched while the working electrode potential was controlled at 0.1 $V_{Ag/AgCl}$. The enrichment of cathodic biofilms was stopped after the cathodic current reached a pseudo-steady state (i.e. when the change in cathodic current was less than 5% for a period of 7 days).

2.3. The kinetics of oxygen reduction

For oxygen reducing cathodic biofilms, DO served as the terminal electron acceptor. To study the effect of DO concentration, we varied the partial pressure of oxygen by mixing the inlet air with pressurized nitrogen gas, while maintaining a constant total inlet pressure. The DO concentration was verified using a DO meter (DO 2700, Oakton Instruments, Vernon Hills, IL, USA). The response of cathodic biofilms to change in partial pressure of oxygen was considered to be at steady-state when the measured current varied by less than 1% for 1 h. The current response was measured for a minimum of 2 h at each of the tested values for oxygen partial pressure.

2.4. Electrochemical methods

Chronomaperometric measurements were used to monitor the cathodic biofilms current during enrichment and characterization studies. A Gamry series 1000™ potentiostat (Gamry Instruments, Warminster, PA, USA) or an in-house custom potentiostat was used to control the working electrode potential during enrichment and measure the resulting current. Gamry series 1000™ potentiostat was used to perform open circuit potential and cyclic voltammetry measurements immediately after inoculation, and after the enrichment stage while varying the partial pressure of oxygen in the inlet gas. Cyclic voltammograms were recorded from 0.5 $V_{Ag/AgCl}$ to −0.5 $V_{Ag/AgCl}$ and then back to 0.5 $V_{Ag/AgCl}$ at a scan rate of 0.010 V/s. Three cycles were recorded for each experimental condition. In general, the 2nd and 3rd cycles showed identical curves, whereas the 1st cycle was different due to the initial contribution of non-Faradaic current. We report the 2nd cycle as representative of cathodic biofilm behavior.

2.5. Mathematical modeling

We used mathematical modeling to describe the kinetics of oxygen reducing cathodic biofilm, and to assess the factors controlling scale up of cathodic biofilm electrodes. A previous report using microelectrodes to measure microscale gradients demonstrated that oxygen reduction on cathodic biofilm electrodes occurs via a two-electron reaction to generate hydrogen peroxide [54]. Two-electron oxygen reduction is assumed to be the primary cathodic reaction in our model. Oxygen reduction to hydrogen peroxide in acidic solutions is described using equation (1) [70,71].

$$O_2 + 2H^+ + 2e^- \rightarrow H_2O_2\ E^o = 0.695 \quad (1)$$

The rate of kinetically controlled electrochemical reactions can be described using Butler-Volmer equation, which includes contribution from forward and reverse reactions to the overall current. Because we set the electrode potential at 0.396 V below the standard reduction potential, the contribution of the anodic reaction to the current is ignored. The contribution of the anodic reaction to the current is less than 1% when the overpotential is less than −0.118 V [70]. Instead of using first order kinetics, we use the Michaelis-Menten equation to describe biologically catalyzed ORR. The details of deriving a combined Michaelis-Menten-Butler-Volmer equation are described in the supplementary information (S1.1). Equation (2) describes the cathodic current density (j_c) as a function of the working electrode potential (ε), DO concentration (S), and temperature (T).

$$j_c = -j_{o_{c,\,max}} \frac{[S]}{K_{M,c} + [S]}\, e^{\frac{-anF(\varepsilon - E - E_L + j_c A R_L)}{RT}} \quad (2)$$

The modified Michaelis-Menten terms are the maximum cathodic current density magnitude ($j_{o_{c,\,max}}$), and the half-saturation constant ($K_{M,c}$). Potential losses are attributed to two terms as described previously: 1) a lumped constant potential loss term (E_L) and 2) an ohmic loss term characterized by a constant ohmic resistance (R_L) [52]. Constant terms in the equation are the number of electrons transferred (n), Faraday's constant (F), electrode surface area (A), and the universal gas constant (R). The transfer coefficient (α) is estimated from the Tafel slope ($b = \frac{\alpha nF\eta}{2.3RT}$). Experimental data for electrode sizes 14.3 cm^2, 40.3 cm^2 and 131 cm^2 are used to estimate the transfer coefficient. Estimates based on experimental data for the 466 cm^2 are omitted due to the high ohmic loss, which causes an underestimation of the transfer coefficient.

Four fitting parameters were calculated by fitting the experimental data describing the current density (j_c) as a function of DO concentration (S) and electrode surface area (A): 1) the maximum cathodic current density magnitude ($j_{o_{c,\,max}}$), 2) the half-saturation constant ($K_{M,c}$), 3) the lumped constant potential loss term (E_L) and 4) the ohmic resistance (R_L). The model was solved to minimize the objective function given in equation (3), where SSD is the sum of squared differences, a is the index (from 1 to 4) for each electrode surface area tested, n_S is the total number of DO concentrations experimentally tested, s is the index for each tested DO concentration, $j_{c_{exp,\,a,s}}$ is the experimentally measured cathodic current density for a given electrode surface area a and DO concentration s, and $j_{c_{calc,\,a,s}}$ is the calculated cathodic current density for and s using the model. All calculations were performed using MATLAB® R2020a.

$$SSD = \sum_{a=1}^{4} \sum_{s=1}^{n_S} (j_{c_{exp,\,a,s}} - j_{c_{calc,\,a,s}}) \quad (3)$$

2.6. Microbial community analysis

2.6.1. Electrode sample preparation

Samples of enriched cathodic biofilms on carbon fiber electrodes were collected to examine the effects of electrode size on the enriched microbial community and to analyze the distribution of the microbial community across electrodes. The electrodes were harvested following the enrichment of cathodic biofilms, indicated by the cathodic current reaching a pseudo steady state. The electrodes were subsampled into grids, with each subsample being 1 cm × 1 cm. For each electrode, several sections of grid were randomly chosen, minced into small particles, and homogenized.

2.6.2. Genomic DNA extraction and 16 S rRNA gene sequencing

For genomic DNA (gDNA) extraction, 200–300 mg of homogenized electrode DNA was extracted using a Qiagen MagAttract PowerMicrobiome kit (QIAGEN, USA). After extraction, samples were quantified using the Quant-iT PicoGreen dsDNA Assay kit. The DNA purifications and libraries were prepared by the University of Michigan Host Microbiome Core as described previously [72]. Briefly, the V4 region of the 16s rRNA gene was amplified from each sample using the dual indexing sequencing strategy developed by Kozich et al. [73]. The polymerase chain reactions were composed and performed as previously described [72].

Amplicon samples were normalized using SequalPrep Normalization Plate Kit (Life technologies) following the manufacturer's protocol for sequential elution. Samples were pooled and the concentration of the pooled samples was determined using Kapa Biosystems Library Quantification kit for Illumina platforms (KapaBiosystems). The sizes of the amplicons in the library are determined using the Agilent Bioanalyzer High Sensitivity DNA analysis kit (Agilent). Libraries and sequencing reagents were prepared according Illumina's protocols ("Preparing Libraries for Sequencing on the MiSeq" and "16 S Sequencing with the Illumina MiSeq Personal Sequencer") as described previously [72]. Amplicons were sequenced on the Illumina MiSeq platform using a MiSeq Reagent 222 kit V2 (catalog no. MS-102-2003) for 500 cycles according to the manufacturer's instructions with modifications for the primer set. FASTQ files were generated for paired end reads.

2.6.3. Analysis of microbiota community

FASTAQ formatted circular consensus sequences were processed and analyzed using mothur v.1.39 [74]. Briefly, filtered sequences were dereplicated and aligned to a newest SILVA-based reference alignment (silva.nr_v132. align) [75]. The sequences were then screened to remove those that did not align to positions 11,894–25,319 of the reference alignment, filtered to remove non-informative columns, preclustered to >99.0% identity (allowing 2 differences), and dereplicated. Chimeras were identified and removed using UCHIME as implemented in mothur v.1.39 in self-referential mode. Filtered sequences were classified against the SILVA (v132) reference taxonomies using a naive Bayesian classifier implemented within mothur [76] with an 80% bootstrap cut-off, and sequences that were not bacteria were removed using remove. lineage. Operational taxonomic units (OTU) were identified using a 97% similarity rate and used for downstream community analyses. OTUs were classified based upon the sequence classifications described above.

3. Results and discussion

In this work, we demonstrated the enrichment of cathodic biofilms that catalyze the ORR at 0.1 $V_{Ag/AgCl}$. The cathodic biofilms were enriched on electrodes of different sizes (14.5 cm^2, 40.3 cm^2, 131 cm^2 and 466 cm^2). The enrichment medium consisted of a dilute municipal wastewater, with an initial bulk COD of 72 ± 5 mg/L. We compared the steady-state current density across the different electrode sizes and investigated the dependency of cathodic current on the bulk concentration of DO under well-mixed conditions. The cathodic biofilms on different sizes were compared using cyclic voltammetry and microbial community analysis.

3.1. Biologically catalyzed oxygen reduction

Cathodic current was observed within the first 5 days of enrichment, and reaches a maximum cathodic current after 15–20 days (data not shown). After the enrichment of cathodic biofilms, the effect of bulk DO concentration on cathodic current density was investigated by varying the bulk DO concentration. As an example, Fig. 1 illustrates the role of the cathodic biofilm in catalyzing the ORR, using the 131 cm^2 electrode. Fig. 1A shows the response of the enriched cathodic biofilm to change in bulk DO concentration. The cathodic current rapidly equilibrated to the change in bulk DO concentration, reaching a pseudo-steady state in less than 30 min. The cathodic current density changed gradually from −65.80 ± 0.11 μA/cm^2 when the bulk DO concentration was 244 μM, to 0.09 ± 0.03 μA/cm^2 when the bulk DO concentration was ~0 μM (the solution was bubbled with pure N_2, and the measured DO concentration was below the detection limit of the DO meter). Fig. 1B shows the kinetics of oxygen reduction on a cathodic biofilm polarized at 0.1 $V_{Ag/AgCl}$ as a function of DO concentration. The kinetics resemble Michaelis-Menten behavior, which can be approximated as first order kinetics for DO concentrations below 71 μM, and zeroth order kinetics for DO concentrations above 195 μM.

We also used cyclic voltammetry to investigate the effect of electrode potential on the cathodic current. Fig. 1C illustrates the role of the enriched cathodic biofilm in catalyzing the ORR by comparing the cyclic voltammograms of: 1) the electrode at 244 μM DO concentration on day 0 – before the enrichment of cathodic biofilm, 2) the enriched biofilm electrode at 244 μM DO concentration on day 40, and 3) the enriched biofilm electrode at ~0 μM DO concentration on day 40. On day 0, a high overpotential for the ORR is observed, with the onset potential of the catalytic wave starting below −0.1 $V_{Ag/AgCl}$. After 40 days of cathodic biofilm enrichment, the cyclic voltammograms show a significant decrease in the overpotential of ORR. The onset potential of the catalytic wave is 0.3 $V_{Ag/AgCl}$, indicating the role of enriched cathodic biofilms in catalyzing oxygen reduction on the cathode. A cathodic peak is observed at −0.17 $V_{Ag/AgCl}$, indicating mass transport limitation at low potentials. The cathodic current decreased significantly when oxygen was removed from the bulk solution by sparging with N_2 gas (~0 μM bulk DO concentration). At −0.17 $V_{Ag/AgCl}$, the cathodic current density on the reduction wave decreased from −135 μA/cm^2 to −10.8 μA/cm^2. Collectively, the cyclic voltammograms show that the observed cathodic current is attributed to ORR which is catalyzed by the enrichment of cathodic biofilms.

3.2. The effect of dissolved oxygen concentration on scale up of enriched cathodic biofilms

The kinetics of oxygen reduction on electrodes of different sizes were investigated by changing the bulk DO concentration. Fig. 2 shows the average steady-steady state current on four electrode sizes (14.5 cm^2, 40.3 cm^2, 131 cm^2 and 466 cm^2) from three biological replicates as function of DO concentration. The dependency of cathodic current on DO concentration resembled Michaelis-Menten kinetics, which can be approximated as first order kinetics at low DO concentrations and zeroth order kinetics at higher DO concentrations. In all tested electrode sizes, the steady-state cathodic current increased linearly with increasing DO concentration in the low range (below 50 μM). The cathodic current plateaus at higher DO concentrations, showing a minimal increase with increasing concentrations above 150 μM. Although the kinetics of oxygen reduction followed a similar pattern across all the tested electrode sizes, the maximum cathodic current density decreased with increasing electrode size. The cathodic current density at 244 μM was −97.0 ± 10.6 μA/cm^2, -76.0 ± 8.2 μA/cm^2, -66.3 ± 3.0 μA/cm^2 and -43.5 ± 10.5 μA/cm^2 for the 14.5 cm^2, 40.3 cm^2, 131 cm^2 and 466 cm^2 electrodes, respectively. Fig. 3A shows that the decrease in current density is proportional to the logarithm of electrode surface area. Dewan et al. documented the logarithmic decrease of MFCs power density with increasing anode surface area in a survey of MFC literature and in pure culture MFCs using lactate oxidation by *Shewanella oneidensis* MR-1 as the anodic reaction [34]. We recently reported similar results with mixed culture wastewater anodic biofilms utilizing wastewater or wastewater amended with potassium acetate as the electron donor [38]. To our knowledge, this is the first study to focus on the scale up of oxygen reducing cathodic biofilms under potentiostatic control. This consistency in the relation between current density and electrode surface area across multiple systems indicates that the scale up of biofilm electrodes may be governed by a similar underlying mechanism that is independent of the microbial community, the direction of electron flow (anodic or cathodic), and the type of terminal electron donor or acceptor.

The steady-state current density as a function of electrode surface area in four selected DO concentrations (12 μM, 73 μM, 171 μM, and 244 μM) is shown in Fig. 3. In all tested DO concentrations, the cathodic current density decreased proportional to the logarithm of the electrode surface area (Fig. 3A). Interestingly, when the current density was normalized to the current density of the 14.5 cm^2 electrode and plotted versus the logarithm of electrode surface area, the linear fit resulted in almost identical slopes (Fig. 3B). This indicates that the factors governing the scalability of oxygen reducing cathodic biofilms are independent of the DO concentrations. Because the scalability of the cathodic biofilms is independent of electron acceptor concentration, it is likely that the scalability is controlled by the design of the electrochemical cell, including the type and distribution of the cathodic biofilm, electrical contact resistance and the electrolyte conductivity.

Cyclic voltammograms provide a secondary evidence to the decrease of current density with increasing electrode size, and provide an insight into the underlying mechanism (Fig. 4). At saturating DO concentration (244 μM), the cathodic current density on the reduction wave at 0.1 $V_{Ag/AgCl}$ was −94.0 μA/cm^2, -64.9 μA/cm^2, -59.9 μA/cm^2 and -51.6 μA/cm^2 for the 14.5 cm^2, 40.3 cm^2, 131 cm^2 and 466 cm^2 electrodes, respectively. This further supports the results obtained from the steady-state kinetic values. In all electrode sizes, the cathodes show an oxygen reduction wave with an onset potential at 0.3 $V_{Ag/AgCl}$. The cathodic

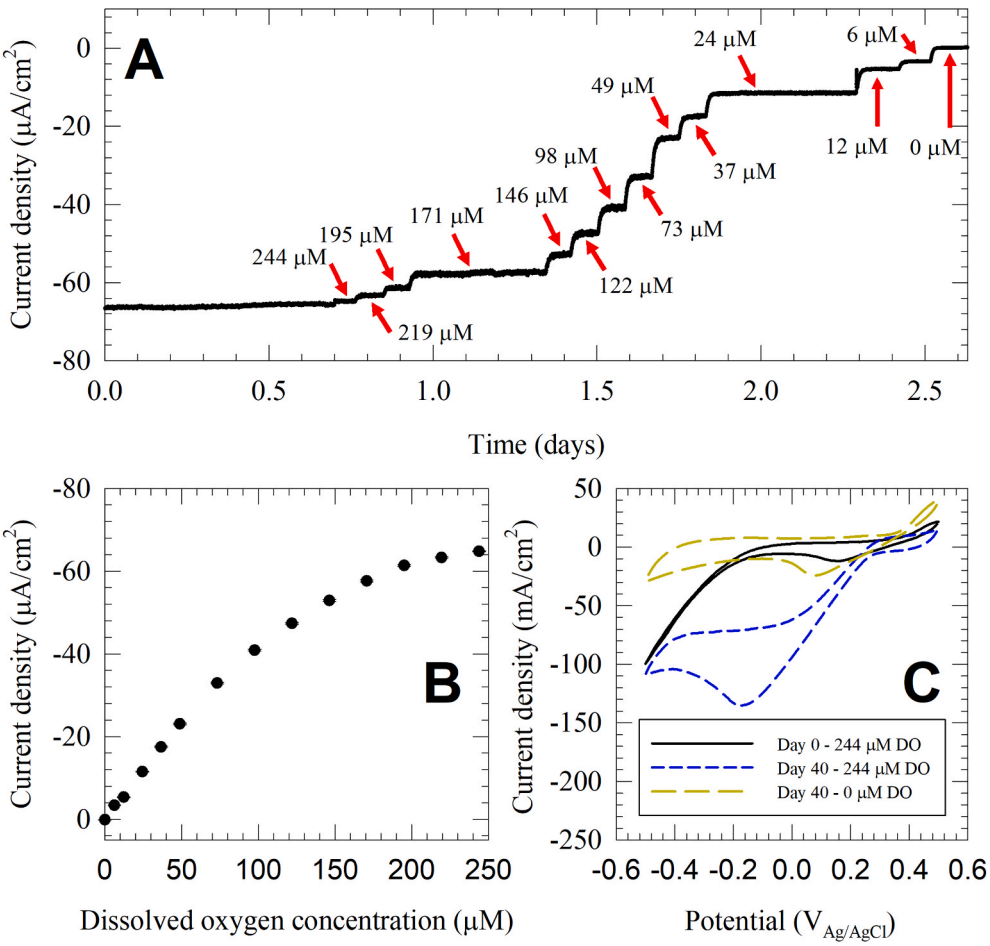

Fig. 1. An example dataset showing current changes as response to change in bulk DO concentration for a biofilm enriched on a 131 cm^2 electrode catalyzing oxygen reduction reaction. A) The response of the cathodic biofilms to change in DO concentration form 244 μM–0 μM. B) The dependency of cathodic current on DO concentration. C) Cyclic voltammograms of the abiotic control (day 0, 244 μM DO concentration), enriched cathodic biofilm in the presence and absence of oxygen (day 40, 244 μM and 0 μM DO concentration, respectively).

current density continues to increase with higher overpotentials until a mass transport peak is reached, beyond which the cyclic voltammograms show a limiting current. The limiting current region is dependent on the DO concentration. For example, in the 14.5 cm^2 cathode, the limiting current region was reached below 0 $V_{Ag/AgCl}$, −0.09 $V_{Ag/AgCl}$, and −0.34 $V_{Ag/AgCl}$ at DO concentrations of 24 μM, 49 μM, and 244 μM, respectively. The 466 cm^2 electrode did not show a limiting current region at the 244 μM DO concentration in the tested potential scan window. When comparing the cyclic voltammograms of each electrode at different DO concentrations, the reduction waves all overlap forming a straight line. The mass transport peak started at different potentials across this line based on the DO concentration. In general, a straight line on the current density-potential curves indicates an uncompensated resistive element dominating the electrochemical processes. The slope of the line was consistent in the voltammograms of all tested electrode sizes. This indicates that the uncompensated ohmic resistance increases linearly with the electrode surface area. Because all the electrode sizes were tested in similar electrochemical cell designs with identical distances between the working and counter electrodes, it is likely the electrical contact resistance or the low ionic conductivity of the medium dominated the resistive element shown in the cyclic voltammograms. Put together, the data suggest that ohmic losses could have played a role in the loss of current density during the scale up of oxygen reducing cathodic biofilms.

3.3. *Mathematical modeling reveals the role of ohmic losses in limiting the scale up of oxygen reducing biofilm electrodes*

Experimental data showed that cathodic current density increased linearly with DO concentration in the low range (below 50 μM), and plateaus at higher concentrations (above 150 μM). This dependency could be explained by Michaelis-Menten kinetics, which are commonly used to describe enzymatically catalyzed biological reactions. However, Michaelis-Menten kinetics do not explain why the maximum current density decreased with increasing electrode surface area. Steady-state current and cyclic voltammograms suggest that a consistent resistive element limits the scale up of cathodic biofilms. We used mathematical modeling to study the factors controlling scale up of cathodic biofilms. By fitting the model equations to the experimental data, we determined the Michaelis-Menten parameters ($j_{o_{c,\,max}}$ and $K_{M,c}$) and estimated the lumped constant potential (E_L) and ohmic resistance terms (R_L).

We combined Michaelis-Menten kinetics with Butler-Volmer equation to describe the dependence of the cathodic current on the electrode potential and DO concentration (equation (2)). Two factors were used to describe potential losses in the system: a lumped constant potential loss term (E_L) and a current-dependent term that is characterized as a constant ohmic resistance (R_L). The objective of the model is to establish one set of parameters to describe the cathodic current density as a function of DO concentration for all electrode sizes tested experimentally. The model input parameters, including experimental parameters and physical constants are detailed in Table 1.

The model fit strongly correlates with the experimental current density data for all electrode sizes, with a coefficient of determination of 0.971. The best fit parameters for the model are reported in Table 2. The model best-fit current alongside the experimental data is shown in Fig. 2. The model slightly underestimates the maximum current density 14.5 cm^2, 131 cm^2 and 466 cm^2 cathodic biofilms while slightly overestimating the maximum current density for the 40.3 cm^2 cathodic biofilm. Experimental considerations could explain the deviation between model fit and experimental data in different electrode sizes,

including the non-uniform solution mixing and differences in the enriched cathodic biofilms. Nevertheless, the model helps to explain the behavior of biofilm cathodes including both the dependency of cathodic current density on DO concentration and on the electrode surface area.

A Michaelis-Menten half-saturation constant of 75.6 μM explains the minimal increase in current density when DO concentration is increased above 150 μM. A lumped constant potential loss of 0.428 V implies an onset potential of 0.466 $V_{Ag/AgCl}$ which is slightly higher than the onset potential observed in the cyclic voltammograms in Fig. 4 (~0.3 $V_{Ag/AgCl}$). The lumped constant potential loss term includes the change in equilibrium potential due to the concentration of reactants and products of the ORR described in equation (1). The change of equilibrium potential due to concentration is described using Nernst's equation. The shift in equilibrium potential due to solution pH accounts for 0.420 V of the lumped constant potential loss term, corresponding to medium pH of 7.1 as opposed to the reduction potential at standard conditions reported in equation (1) (pH = 0). The additional shift in equilibrium potential is expected due to DO and H_2O_2 concentrations. However, this shift could not be estimated because H_2O_2 concentration in the reactor or near the electrode surface was unknown. The low transfer coefficient value (α = 0.234) contributes to the asymmetry of the current-overpotential curve, moving the cathodic onset potential to be experimentally observed at a lower potential. Based on the model, ohmic loss explains the decrease of cathodic current density with increasing electrode surface area. Larger electrodes pass higher overall current, and thus exhibit higher ohmic loss (*i*R). An ohmic resistance of 2.80 Ω causes a 58.3% decrease in current density when increasing the electrode surface area by a factor of 32 (from 14.5 cm^2 to 466 cm^2). There was no decrease in cathodic current density when computing the model with the same fitting parameters in Table 2 while setting the ohmic resistance to zero. This confirms that ohmic resistance is the main factor controlling the decrease in cathodic current density with increasing electrode surface area.

Several experimental factors contribute to ohmic resistance. In our experiments, we verified that the contact resistance between the potentiostat leads and any point on the working electrode surface is below 1 Ω. High contact resistance is an important consideration when working with inexpensive carbon electrodes, such as the carbon cloth electrodes used in our system. To minimize the overall contact resistance, we constructed the electrodes with multiple contact points with the current collector wire which has a higher conductivity compared to the carbon cloth material. The remaining ohmic resistance could be attributed to the electrolytic solution resistance, especially considering the low ionic strength in the diluted wastewater medium used in our experiments. The contribution of solution resistance to ohmic losses was minimized by decreasing the distance between the reference electrode and working electrode to ~0.6 cm. It should be noted that the average distance between the reference electrode and the working electrode

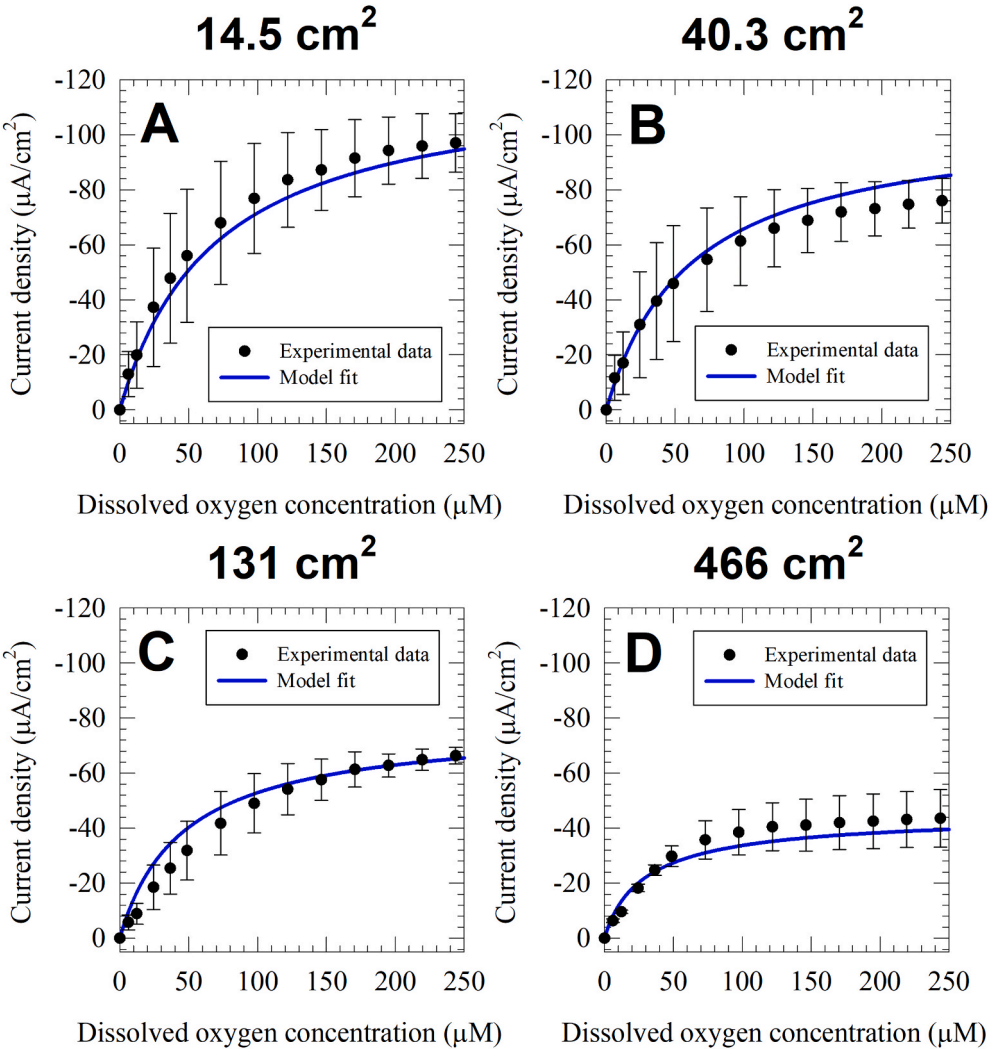

Fig. 2. Experimental and model best-fit current of oxygen reducing cathodic biofilms in response to change in DO concentration from 244 μM to 0 μM, A) 14.5 cm^2, B) 40.3 cm^2, C) 131 cm^2, and D) 466 cm^2. The data represent the average of three biological replicates, and the error bars represent the standard deviation.

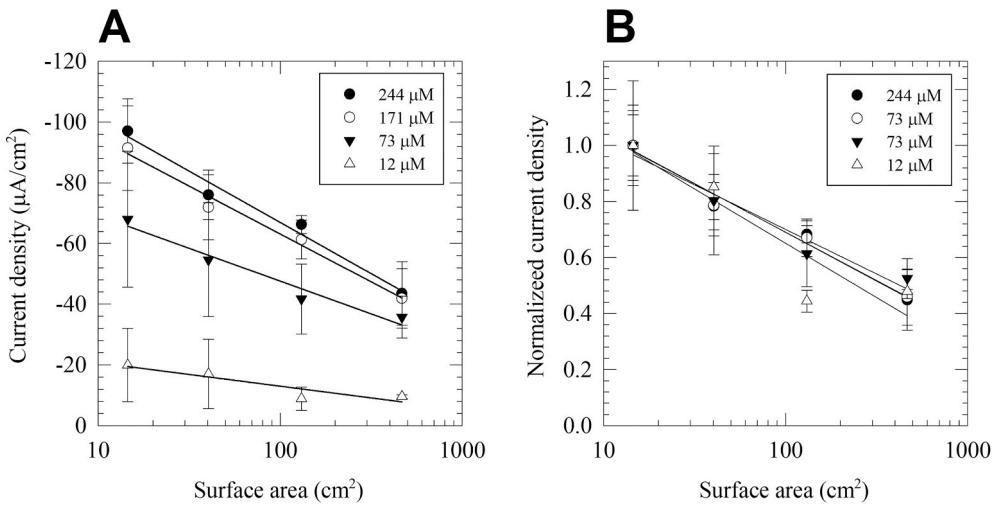

Fig. 3. (A) The current density of oxygen reducing cathodic biofilms (surface areas = 14.5 cm^2, 40.3 cm^2, 131 cm^2 and 466 cm^2) to change in DO concentration. (B) The current density normalized to the current density of the 14.5 cm^2 cathodic biofilm at each concentration. This figure shows that current density loss due to scale up is similar, regardless of DO concentration. The data represent the average of three biological replicates, and the error bars represent the standard deviation.

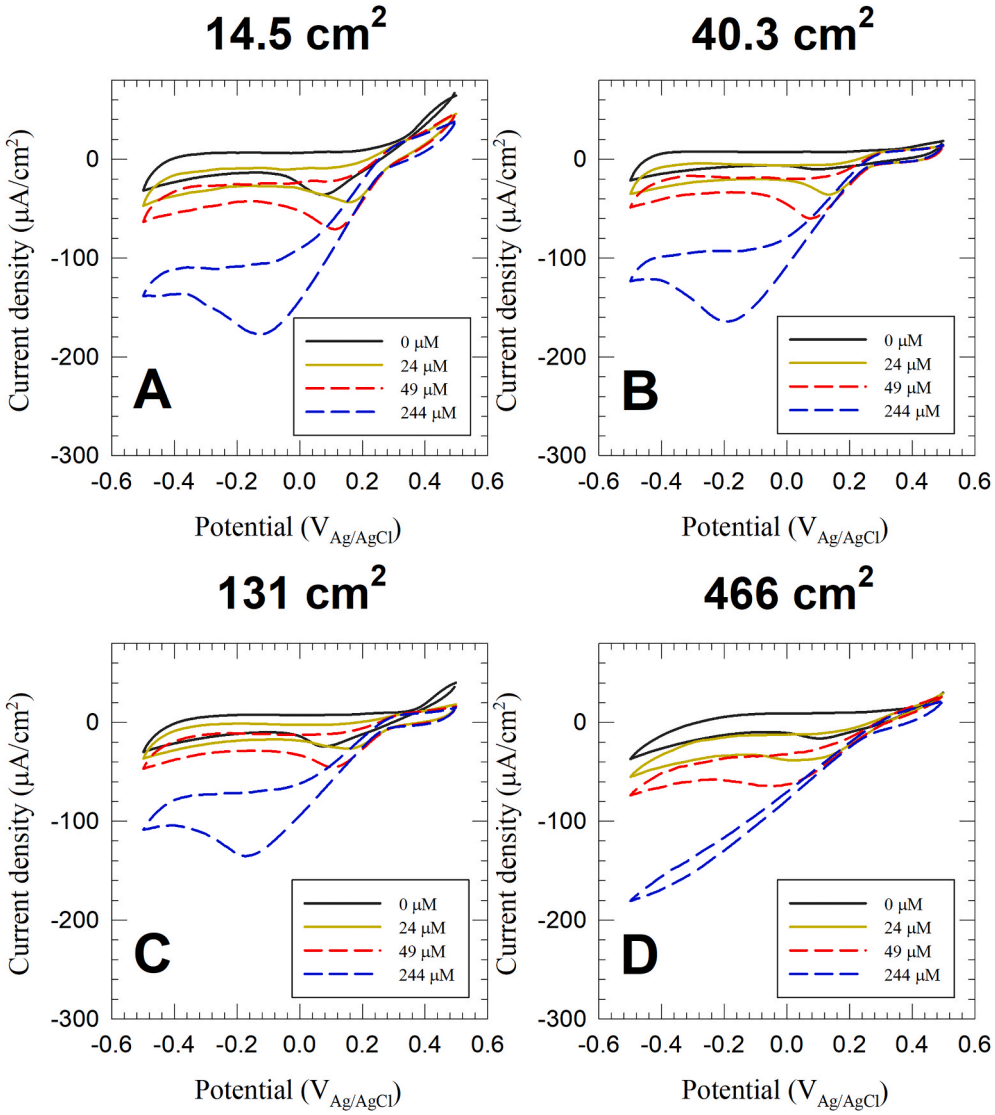

Fig. 4. Representative cyclic voltammograms of oxygen reducing cathodic biofilms (surface areas: A) 14.5 cm^2, B) 40.3 cm^2, C) 131 cm^2, and D) 466 cm^2) at select DO concentrations 244 μM–0 μM. The data is a representative example selected from three biological replicates.

Table 1
Model input parameters for oxygen reduction reaction. The working electrode surface area (A) working electrode potential (ε) and temperature (T) are independent variables.

Description	Parameter	Value	Unit	Reference
Area	A	0.0015, 0.0040, 0.0131, 0.0466	m^2	This work
Applied potential	ε	0.299	V	This work
Temperature	T	296.15	K	This work
Standard reduction potential	E	0.695	V	[70]
Number of electrons transferred	n	2	Unitless	[54]
Universal gas constant	R	8.314472	$J\ K^{-1}\ mol^{-1}$	[77]
Faraday's constant	F	96485.3399	$s\ A\ mol^{-1}$	[77]
Transfer coefficient	α	0.234	Unitless	This work

Table 2
Model fitting parameters and coefficient of determination.

Description	Parameter	Value	Unit
Maximum cathodic current density	$j_{o_{c,\ max}}$	2.402	$A\ m^{-2}$
Half-saturation constant	$K_{M,c}$	75.6	μM
Lumped constant potential loss	E_L	0.428	V
Resistance responsible for ohmic loss	R_L	2.80	Ω
Coefficient of determination	R^2	0.971	Unitless

surface is inevitably larger for large electrodes. This could result in a variable solution resistance that is dependent on the electrode size. The assumption of a constant ohmic resistance term for all electrode sizes tested is a limitation to our model. Despite our effort to design the biofilm reactors to minimize ohmic losses, we still observed a 58.3% decrease in current density when increasing the electrode surface area by a factor of 32. Further reactor design improvements could decrease the ohmic losses. This includes decreasing the contact resistance by using mesh current collector or using an electrode material with higher electrical conductivity. Solution resistance could be decreased by increasing the ionic strength of the medium. However, significantly increasing the ionic strength above the physiological range where microbes can grow could be detrimental to the development and the activity of EABs. As demonstrated here, mathematical modeling can be used as a guide to design and scale up biofilm electrodes for microbial electrochemical technology applications.

3.4. Microbial community analysis

After the enrichment of cathodic biofilms and investigating the effect of bulk DO concentration on the performance of cathodes, we collected the cathodic biofilm samples to analyze the microbial community structure. The microbial community analysis aimed to answer two questions: 1) is there a significant difference in the microbial community structure enriched on different electrode sizes? 2) do we observe significant heterogeneity in microbial community structure across the electrode surface? The first question addresses whether or not we can attribute the difference in cathodic biofilm behavior on different electrode sizes to a difference in microbial community structure. The second question addresses whether large electrodes are negatively affected by non-uniform enrichment across the electrode surface. One reason for this is if the medium was not well-mixed which results in the stratification of DO concentration along the height of the reactor. Since the enriched cathodic biofilms use DO as a soluble electron acceptor, stratification in DO concentration is expected to cause a change in microbial community structure along with the height of the electrode. Another reason could be due to the large size of the electrodes allowing a higher probability for different microbial cells to initially colonize the electrode surface to create heterogeneity. To test this, we sampled the largest electrode in four different regions (top, middle top, middle bottom, and bottom) and compared the structure of the microbial community.

The microbial community analysis on both class and genus levels revealed that the microbial community structure is unlikely to be the primary cause for the difference in cathodic biofilm behavior across different electrode sizes, or to have a significant heterogeneity across a single electrode. Fig. 5 shows the microbial community structure across four electrode sizes (14.5 cm^2, 40.3 cm^2, 131 cm^2 and 466 cm^2), and across four regions of the 466 cm^2 electrode (class level analysis is included in the supplementary information, Fig. S2). On the class level, *gammaproteobacteria* accounted for the highest relative abundance across all samples (26.8%–40.2%), followed by *alphaproteobacteria* (18.6%–22.2%), *bacteroidia* (9.8%–15.1%) and *planctomycetacia* (8.6%–13.6%). On the genus level (Fig. 5), all electrodes were dominated by an unclassified *gammaproteobacteria* (20.9%–35.8%), followed by *Terrimonas* (1.2%–4.9%), uncultured *rubinisphaeraceae* (1.5%–4.2%), uncultured *pirellulaceae* (1.6%–3.4%), and *hyphomonadaceae (SWB02)* (0.6%–3.6%). No other genus accounted for an average relative abundance higher than 2%. The closest cultured relatives to the unclassified *gammaproteobacteria* were *Arenicella xantha* strain KMM 3895 [78] and *Pseudomonas lactis* strain DSM 29167 [79], sharing 90.91% and 90.51% identity, respectively. Neither strain have been previously reported to grow on electrodes. To the authors' knowledge, there are no cultured *Terrimonas* species, or species belonging to the *rubinisphaeraceae*, *pirellulaceae*, or *hyphomonadaceae* families are known to exchange electrons with solid electrodes, anodically or cathodically. This highlights the need to isolate and study aerobic electrochemically-active microorganisms. A review paper published in 2016 which reviewed isolated microorganisms capable of forming EABs reported six aerobic species out of 45 that were capable of cathodic extracellular electron transfer [7].

No clear correlation was observed to support the differentiation of microbial community structure based on the electrode size or across the height of the electrode in the dominant bacterial groups (Fig. 5). However, few groups showed a correlation between relative abundance and electrode size (14.5 cm^2, 40.3 cm^2, 131 cm^2 and 466 cm^2), or location within the 466 cm^2 electrode (top, middle top, middle bottom, and bottom). On the class level, the relative abundance of *planctomycetacia* increased with decreasing electrode size (13.6%, 12.0%, 11.2%, 10.0%), while the relative abundance of *alphaproteobacteria* decreased along the height of the 466 cm^2 electrode (22.2%, 21.5%, 20.2%, 19.7%). On the genus level, the relative abundance of both the uncultured *rubinisphaeraceae* and *hyphomonadaceae (SWB02)* increased with decreasing electrode size (4.2%, 3.4%, 2.2%, 1.6% and 3.6%, 2.5%, 1.0%, 1.0%, respectively), while *hyphomonadaceae (SWB02)* also decreased along the height of the electrode (0.9%, 0.9%, 0.8%, 0.6%). It is unlikely that such correlation explains a function difference in the different cathodic biofilms. The maximum range of variability in the groups that showed a correlation with electrode size, or along the electrode height is 3.6%, which is well below the variability in the dominant groups in both the class level (*gammaproteobacteria*; 13.4%) and the genus level (unclassified *gammaproteobacteria*; 14.9%).

Overall, the microbial community analysis revealed limited differences in the microbial community structure relative to the electrode size or the location within the electrode, suggesting that the microbial community does not cause the decrease in cathodic current density with increasing electrode surface area. However, despite the consistent microbial community structure across the tested electrode sizes and locations, the enriched species are not known to form cathodic EABs. We attributed this to the limited knowledge of the species forming oxygen-reducing cathodic biofilms and the underlying mechanisms, which warrants further research about the identity, roles and mechanisms of these microbial populations.

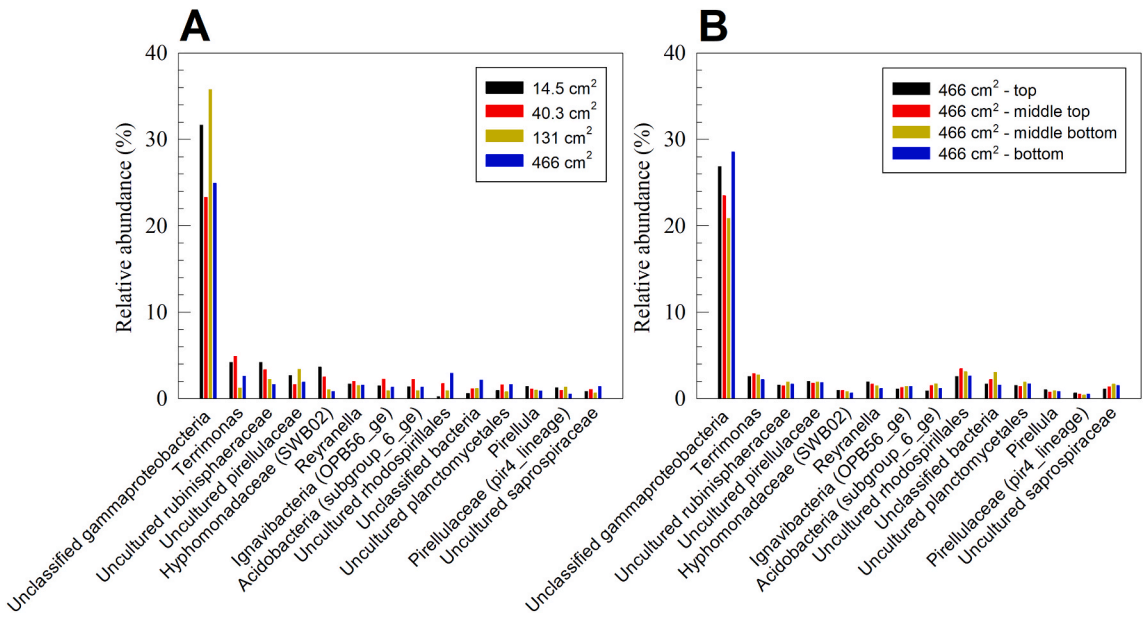

Fig. 5. Genus-level 16 S rRNA gene microbial community analysis of A) four oxygen-reducing cathodic biofilms (surface areas = 14.5 cm^2, 40.3 cm^2, 131 cm^2 and 466 cm^2), and B) 466 cm^2 cathodic biofilm sampled at four different locations. The data show that the microbial community structure is independent of cathode size, and of the location within the cathode.

4. Conclusions

In this work, we investigated the factors affecting the scale up of oxygen reducing cathodic biofilms. To do this, we enriched mixed culture cathodic biofilms on electrodes of four different sizes (14.5 cm^2, 40.3 cm^2, 131 cm^2 and 466 cm^2). We found that:

- The enrichment of biofilms catalyzed oxygen reduction reaction, changing the onset potential from −0.1 $V_{Ag/AgCl}$ at the start of the experiments to 0.3 $V_{Ag/AgCl}$ after the enrichment.
- By changing the bulk dissolved oxygen concentration, we showed that oxygen reduction in cathodic biofilms followed Michaelis-Menten kinetics regardless of the electrode surface area.
- The cathodic current density decreased proportional to the logarithm of electrode surface area.
- The loss of cathodic current density during scale up was independent of electron acceptor concentration.
- Cyclic voltammograms show that the cathodic current density is controlled by a resistive element that is consistent across all the tested electrode sizes.
- Mathematical modeling using a combined Michaelis-Menten and Butler-Volmer model indicates that ohmic losses limit the scale up of cathodic biofilms.
- The microbial community analysis revealed that the microbial community structure was independent of the electrode size, and of the location within the electrode. This suggests that the microbial community structure did not contribute to the poor scalability of oxygen reducing cathodic biofilms.

CRediT authorship contribution statement

Abdelrhman Mohamed: Conceptualization, Formal analysis, Investigation, Methodology, Visualization, Writing – original draft. **Phuc T. Ha:** Data curation, Formal analysis, Writing – review & editing. **Haluk Beyenal:** Conceptualization, Methodology, Funding acquisition, Supervision, Writing – review & editing.

Declaration of competing interest

The authors declare that the research was conducted in the absence of any commercial or financial relationships that could be construed as a potential conflict of interest.

Acknowledgments

This research was supported by the Office of Naval Research award number N000141512471 and the National Science Foundation award number 1706889. The authors thank the staff at the Moscow Water Reclamation and Reuse Facility (Moscow, ID) for logistical assistance for providing wastewater and mixed-culture inoculum. The authors acknowledge Secil Tutar and Hannah M. Zmuda for their assistance with reactor construction and experiment operation.

Appendix A. Supplementary data

Supplementary data to this article can be found online at https://doi.org/10.1016/j.bioflm.2021.100053.

References

[1] Rabaey K. Bioelectrochemical systems: from extracellular electron transfer to biotechnological application, 8. Water Intelligence Online; 2009. https://doi.org/10.2166/9781780401621.
[2] Beyenal H, Babauta J. Biofilms in bioelectrochemical systems. John Wiley & Sons, Inc; 2015.
[3] Schröder U, Harnisch F, Angenent LT. Microbial electrochemistry and technology: terminology and classification. Energy Environ Sci 2015;8(2):513–9. https://doi.org/10.1039/c4ee03359k.
[4] Lovley DR, Nevin KP. A shift in the current: new applications and concepts for microbe-electrode electron exchange. Curr Opin Biotechnol 2011;22(3):441–8. https://doi.org/10.1016/j.copbio.2011.01.009.
[5] Babauta J, et al. Electrochemically active biofilms: facts and fiction. *A review.* Biofouling 2012;28(8):789–812. https://doi.org/10.1080/08927014.2012.710324.
[6] Shi L, et al. Extracellular electron transfer mechanisms between microorganisms and minerals. Nat Rev Microbiol 2016;14(10):651–62. https://doi.org/10.1038/nrmicro.2016.93.
[7] Koch C, Harnisch F. Is there a specific ecological niche for electroactive microorganisms? ChemElectroChem 2016;3(9):1282–95. https://doi.org/10.1002/celc.201600079.

[8] Logan BE, et al. Microbial fuel cells: methodology and technology. Environ Sci Technol 2006;40(17):5181–92. https://doi.org/10.1021/es0605016.

[9] Santoro C, et al. Microbial fuel cells: from fundamentals to applications. A review. J Power Sources 2017;356:225–44. https://doi.org/10.1016/j.jpowsour.2017.03.109.

[10] Stirling JL, et al. Microbial fuel cells. Biochem Soc Trans 1983;11(4):451–3. https://doi.org/10.1042/bst0110451.

[11] Allen RM, Bennetto HP. Microbial fuel-cells. Appl Biochem Biotechnol 1993;39–40 (1):27–40. https://doi.org/10.1007/bf02918975.

[12] Dong Y, et al. A 90-liter stackable baffled microbial fuel cell for brewery wastewater treatment based on energy self-sufficient mode. Bioresour Technol 2015;195:66–72. https://doi.org/10.1016/j.biortech.2015.06.026.

[13] Ewing T, et al. Self-powered wastewater treatment for the enhanced operation of a facultative lagoon. J Power Sources 2014;269:284–92. https://doi.org/10.1016/j.jpowsour.2014.06.114.

[14] Reimers CE, et al. Microbial fuel cell energy from an ocean cold seep. Geobiology 2006;4(2):123–36. https://doi.org/10.1111/j.1472-4669.2006.00071.x.

[15] Girguis PR, Nielsen ME, Figueroa I. Harnessing energy from marine productivity using bioelectrochemical systems. Curr Opin Biotechnol 2010;21(3):252–8. https://doi.org/10.1016/j.copbio.2010.03.015.

[16] Kagan J, Hsu L, Chadwick B. Large-scale benthic microbial fuel cell construction, deployment, and operation. In: Beyenal H, Babauta J, editors. Biofilms in bioelectrochemical systems: from laboratory practice to data interpretation. John Wiley & Sons, Inc; 2015.

[17] Abrevaya XC, et al. Analytical applications of microbial fuel cells. Part II: toxicity, microbial activity and quantification, single analyte detection and other uses. Biosens Bioelectron 2015;63:591–601. https://doi.org/10.1016/j.bios.2014.04.053.

[18] Donovan C, et al. Sediment microbial fuel cell powering a submersible ultrasonic receiver: new approach to remote monitoring. J Power Sources 2013;233:79–85. https://doi.org/10.1016/j.jpowsour.2012.12.112.

[19] Lovley DR, Nevin KP. Electrobiocommodities: powering microbial production of fuels and commodity chemicals from carbon dioxide with electricity. Curr Opin Biotechnol 2013;24(3):385–90. https://doi.org/10.1016/j.copbio.2013.02.012.

[20] Rabaey K, Rozendal RA. Microbial electrosynthesis - revisiting the electrical route for microbial production. Nat Rev Microbiol 2010;8(10):706–16. https://doi.org/10.1038/nrmicro2422.

[21] Lu L, Ren ZJ. Microbial electrolysis cells for waste biorefinery: a state of the art review. Bioresour Technol 2016;215:254–64. https://doi.org/10.1016/j.biortech.2016.03.034.

[22] Logan BE, et al. Microbial electrolysis cells for high yield hydrogen gas production from organic matter. Environ Sci Technol 2008;42(23):8630–40. https://doi.org/10.1021/es801553z.

[23] Cheng S, et al. Direct biological conversion of electrical current into methane by electromethanogenesis. Environ Sci Technol 2009;43(10):3953–8. https://doi.org/10.1021/es803531g.

[24] Speers AM, Young JM, Reguera G. Fermentation of glycerol into ethanol in a microbial electrolysis cell driven by a customized consortium. Environ Sci Technol 2014;48(11):6350–8. https://doi.org/10.1021/es500690a.

[25] Rozendal RA, et al. Efficient hydrogen peroxide generation from organic matter in a bioelectrochemical system. Electrochem Commun 2009;11(9):1752–5. https://doi.org/10.1016/j.elecom.2009.07.008.

[26] Lu L, et al. Enhanced bioremediation of hydrocarbon-contaminated soil using pilot-scale bioelectrochemical systems. J Hazard Mater 2014;274:8–15. https://doi.org/10.1016/j.jhazmat.2014.03.060.

[27] Pous N, et al. Bioremediation of nitrate-polluted groundwater in a microbial fuel cell. J Chem Technol Biotechnol 2013;88(9):1690–6. https://doi.org/10.1002/jctb.4020.

[28] Zhou M, Wang W, Chi M. Enhancement on the simultaneous removal of nitrate and organic pollutants from groundwater by a three-dimensional bio-electrochemical reactor. Bioresour Technol 2009;100(20):4662–8. https://doi.org/10.1016/j.biortech.2009.05.002.

[29] Chen X, et al. Self-sustaining advanced wastewater purification and simultaneous in situ nutrient recovery in a novel bioelectrochemical system. Chem Eng J 2017;330:692–7. https://doi.org/10.1016/j.cej.2017.07.130.

[30] Nancharaiah YV, Venkata Mohan S, Lens PN. Metals removal and recovery in bioelectrochemical systems: a review. Bioresour Technol 2015;195:102–14. https://doi.org/10.1016/j.biortech.2015.06.058.

[31] Wu S, et al. A novel pilot-scale stacked microbial fuel cell for efficient electricity generation and wastewater treatment. Water Res 2016;98:396–403. https://doi.org/10.1016/j.watres.2016.04.043.

[32] Heidrich ES, et al. Performance of a pilot scale microbial electrolysis cell fed on domestic wastewater at ambient temperatures for a 12 month period. Bioresour Technol 2014;173:87–95. https://doi.org/10.1016/j.biortech.2014.09.083.

[33] Cusick RD, et al. Performance of a pilot-scale continuous flow microbial electrolysis cell fed winery wastewater. Appl Microbiol Biotechnol 2011;89(6):2053–63. https://doi.org/10.1007/s00253-011-3130-9.

[34] Dewan A, Beyenal H, Lewandowski Z. Scaling up microbial fuel cells. Environ Sci Technol 2008;42(20):7643–8. https://doi.org/10.1021/es800775d.

[35] Hsu L, et al. Scale up considerations for sediment microbial fuel cells. RSC Adv 2013;3(36):15947–54. https://doi.org/10.1039/c3ra43180k.

[36] Martinucci E, et al. Energy balance and microbial fuel cells experimentation at wastewater treatment plant Milano-Nosedo. Int J Hydrogen Energy 2015;40(42):14683–9. https://doi.org/10.1016/j.ijhydene.2015.08.100.

[37] Walter XA, et al. From single MFC to cascade configuration: the relationship between size, hydraulic retention time and power density. Sustainable Energy Technologies and Assessments 2016;14:74–9. https://doi.org/10.1016/j.seta.2016.01.006.

[38] Tutar S, et al. Electron donor availability controls scale up of anodic biofilms. Bioelectrochemistry 2020;132. https://doi.org/10.1016/j.bioelechem.2019.107403. 107403.

[39] Zhuang L, et al. Long-term evaluation of a 10-liter serpentine-type microbial fuel cell stack treating brewery wastewater. Bioresour Technol 2012;123:406–12. https://doi.org/10.1016/j.biortech.2012.07.038.

[40] Zhuang L, et al. Scalable microbial fuel cell (MFC) stack for continuous real wastewater treatment. Bioresour Technol 2012;106:82–8. https://doi.org/10.1016/j.biortech.2011.11.019.

[41] Ieropoulos I, Greenman J, Melhuish C. Microbial fuel cells based on carbon veil electrodes: stack configuration and scalability. Int J Energy Res 2008;32(13):1228–40. https://doi.org/10.1002/er.1419.

[42] Aelterman P, et al. Continuous electricity generation at high voltages and currents using stacked microbial fuel cells. Environ Sci Technol 2006;40(10):3388–94. https://doi.org/10.1021/es0525511.

[43] Zhuang L, Zhou SG. Substrate cross-conduction effect on the performance of serially connected microbial fuel cell stack. Electrochem Commun 2009;11(5):937–40. https://doi.org/10.1016/j.elecom.2009.02.027.

[44] Oh SE, Logan BE. Voltage reversal during microbial fuel cell stack operation. J Power Sources 2007;167(1):11–7. https://doi.org/10.1016/j.jpowsour.2007.02.016.

[45] Ewing T, et al. Scale-up of sediment microbial fuel cells. J Power Sources 2014;272:311–9. https://doi.org/10.1016/j.jpowsour.2014.08.070.

[46] Ledezma P, Greenman J, Ieropoulos I. MFC-cascade stacks maximise COD reduction and avoid voltage reversal under adverse conditions. Bioresour Technol 2013;134:158–65. https://doi.org/10.1016/j.biortech.2013.01.119.

[47] Papaharalabos G, et al. Autonomous energy harvesting and prevention of cell reversal in MFC stacks. J Electrochem Soc 2016;164(3):H3047–51. https://doi.org/10.1149/2.0081703jes.

[48] Zhang Y, Angelidaki I. Self-stacked submersible microbial fuel cell (SSMFC) for improved remote power generation from lake sediments. Biosens Bioelectron 2012;35(1):265–70. https://doi.org/10.1016/j.bios.2012.02.059.

[49] Kim B, et al. Controlling voltage reversal in microbial fuel cells. Trends Biotechnol 2020;38(6):667–78. https://doi.org/10.1016/j.tibtech.2019.12.007.

[50] Babauta JT, et al. Scaling up benthic microbial fuel cells using flyback converters. J Power Sources 2018;395:98–105. https://doi.org/10.1016/j.jpowsour.2018.05.042.

[51] Freguia S, et al. Non-catalyzed cathodic oxygen reduction at graphite granules in microbial fuel cells. Electrochim Acta 2007;53(2):598–603. https://doi.org/10.1016/j.electacta.2007.07.037.

[52] Renslow R, et al. Oxygen reduction kinetics on graphite cathodes in sediment microbial fuel cells. Phys Chem Chem Phys 2011;13(48):21573–84. https://doi.org/10.1039/c1cp23200b.

[53] Ter Heijne A, et al. Cathode potential and mass transfer determine performance of oxygen reducing biocathodes in microbial fuel cells. Environ Sci Technol 2010;44(18):7151–6. https://doi.org/10.1021/es100950t.

[54] Babauta JT, et al. Microscale gradients of oxygen, hydrogen peroxide, and pH in freshwater cathodic biofilms. ChemSusChem 2013;6(7):1252–61. https://doi.org/10.1002/cssc.201300019.

[55] Erable B, Feron D, Bergel A. Microbial catalysis of the oxygen reduction reaction for microbial fuel cells: a review. ChemSusChem 2012;5(6):975–87. https://doi.org/10.1002/cssc.201100836.

[56] Bergel A, Féron D, Mollica A. Catalysis of oxygen reduction in PEM fuel cell by seawater biofilm. Electrochem Commun 2005;7(9):900–4. https://doi.org/10.1016/j.elecom.2005.06.006.

[57] Liang P, et al. Evaluation of applied cathode potential to enhance biocathode in microbial fuel cells. J Chem Tech Biotechnol 2009;84(5):794–9. https://doi.org/10.1002/jctb.2114.

[58] Rabaey K, et al. Cathodic oxygen reduction catalyzed by bacteria in microbial fuel cells. ISME J 2008;2(5):519–27. https://doi.org/10.1038/ismej.2008.1.

[59] Rimboud M, et al. Different methods used to form oxygen reducing biocathodes lead to different biomass quantities, bacterial communities, and electrochemical kinetics. Bioelectrochemistry 2017;116:24–32. https://doi.org/10.1016/j.bioelechem.2017.03.001.

[60] He Z, Angenent LT. Application of bacterial biocathodes in microbial fuel cells. Electroanalysis 2006;18(19–20):2009–15. https://doi.org/10.1002/elan.200603628.

[61] Clauwaert P, et al. Biological denitrification in microbial fuel cells. Environ Sci Technol 2007;41(9):3354–60. https://doi.org/10.1021/es062580r.

[62] Cao X, et al. A completely anoxic microbial fuel cell using a photo-biocathode for cathodic carbon dioxide reduction. Energy Environ Sci 2009;2(5). https://doi.org/10.1039/b901069f.

[63] Thrash JC, et al. Electrochemical stimulation of microbial perchlorate reduction. Environ Sci Technol 2007;41(5):1740–6. https://doi.org/10.1021/es062772m.

[64] Dominguez-Benetton X, et al. Metal recovery by microbial electro-metallurgy. Prog Mater Sci 2018;94:435–61. https://doi.org/10.1016/j.pmatsci.2018.01.007.

[65] Wang H, Ren ZJ. Bioelectrochemical metal recovery from wastewater: a review. Water Res 2014;66:219–32. https://doi.org/10.1016/j.watres.2014.08.013.

[66] Jiang Y, et al. A novel microbial fuel cell sensor with biocathode sensing element. Biosens Bioelectron 2017;94:344–50. https://doi.org/10.1016/j.bios.2017.02.052.

[67] Cristiani P, Mollica A. On-line biofilm monitoring by "BIOX" electrochemical probe. Water Sci Technol 2003;47(5):45–9. https://doi.org/10.2166/wst.2003.0277.

[68] Pavanello G, et al. Exploiting a new electrochemical sensor for biofilm monitoring and water treatment optimization. Water Res 2011;45(4):1651–8. https://doi.org/10.1016/j.watres.2010.12.003.
[69] Lewandowski Z, Beyenal H. Fundamentals of biofilm research. second ed. CRC Press; 2017.
[70] Bard AJ, Faulkner LR. Electrochemical methods: fundamentals and applications. second ed. Wiley; 2008. p. 864.
[71] Vetter KJ. Electrochemical kinetics; theoretical aspects (translation of electrochemische kinetik by springer-verlag). Academic Press; 1967.
[72] Seekatz AM, et al. Fecal microbiota transplantation eliminates Clostridium difficile in a murine model of relapsing disease. Infect Immun 2015;83(10):3838–46. https://doi.org/10.1128/IAI.00459-15.
[73] Kozich JJ, et al. Development of a dual-index sequencing strategy and curation pipeline for analyzing amplicon sequence data on the MiSeq Illumina sequencing platform. Appl Environ Microbiol 2013;79(17):5112–20. https://doi.org/10.1128/AEM.01043-13.
[74] Schloss PD, et al. Introducing mothur: open-source, platform-independent, community-supported software for describing and comparing microbial communities. Appl Environ Microbiol 2009;75(23):7537–41. https://doi.org/10.1128/AEM.01541-09.
[75] Pruesse E, et al. SILVA: a comprehensive online resource for quality checked and aligned ribosomal RNA sequence data compatible with ARB. Nucleic Acids Res 2007;35(21):7188–96. https://doi.org/10.1093/nar/gkm864.
[76] Wang Q, et al. Naive Bayesian classifier for rapid assignment of rRNA sequences into the new bacterial taxonomy. Appl Environ Microbiol 2007;73(16):5261–7. https://doi.org/10.1128/AEM.00062-07.
[77] Mohr PJ, Taylor BN, Newell DB. CODATA recommended values of the fundamental physical constants: 2006. Rev Mod Phys 2008;80(2):633–730. https://doi.org/10.1103/RevModPhys.80.633.
[78] Romanenko LA, et al. Arenicella xantha gen. nov., sp. nov., a gammaproteobacterium isolated from a marine sandy sediment. Int J Syst Evol Microbiol 2010;60(Pt 8):1832–6. https://doi.org/10.1099/ijs.0.017194-0.
[79] von Neubeck M, et al. Pseudomonas lactis sp. nov. and Pseudomonas paralactis sp. nov., isolated from bovine raw milk. Int J Syst Evol Microbiol 2017;67(6):1656–64. https://doi.org/10.1099/ijsem.0.001836.